



Article

# A Novel Expanding Mechanism of Gastrointestinal Microrobot: Design, Analysis and Optimization

Wei Wang <sup>1,2</sup> , Guozheng Yan <sup>1,2,\*</sup>, Zhiwu Wang <sup>1,2</sup>, Pingping Jiang <sup>1,2</sup>, Yicun Meng <sup>1,2</sup>, Fanji Chen <sup>1,2</sup> and Rongrong Xue <sup>1,2</sup>

<sup>1</sup> School of electronic information and electrical engineering, Shanghai Jiao Tong University, Shanghai 200240, China; aries-wang@sjtu.edu.cn (W.W.); zwwang@sjtu.edu.cn (Z.W.); jpp99@sjtu.edu.cn (P.J.); yicun.meng@sjtu.edu.cn (Y.M.); cfj0717@sjtu.edu.cn (F.C.); rongrongxue@sjtu.edu.cn (R.X.)

<sup>2</sup> Institute of Medical Robotics, Shanghai Jiao Tong University, Shanghai 200240, China

\* Correspondence: gzhyan@sjtu.edu.cn

Received: 13 September 2019; Accepted: 24 October 2019; Published: 26 October 2019



**Abstract:** In order to make the gastrointestinal microrobot (GMR) expand and anchor in the gastrointestinal tract reliably, a novel expanding mechanism of the GMR is proposed in this paper. The overlapping expanding arm is designed to be used to increase the variable diameter ratio (ratio of fully expanded diameter to fully folded diameter) to 3.3, which makes the robot more adaptable to the intestinal tract of different sections of the human body. The double-layer structure of the expanding arm increases the contact area with the intestine, reducing the risk of intestinal damage. The kinematics and mechanical model of the expanding arm are established, and the rigid velocity, rigid acceleration, and expanding force of the expanding arm are analyzed. The elastodynamics model of the expanding arm is established. Through the finite element analysis (FEA), the velocity, acceleration, and the value and distribution of the stress of the expanding arm under elastic deformation are obtained. Based on the elastodynamics analysis, the structure of the expanding arm is optimized. By the structure optimization, the thickness of the expanding mechanism is reduced by 0.4mm, the weight is reduced by 31%, and the stress distribution is more uniform. Through the mechanical test, the minimum expanding force of the expanding mechanism is 1.3 N and the maximum expanding force is 6.5 N. Finally, the robot is tested in the rigid pipeline and the isolated intestine to verify the reliability and safety of the expanding mechanism.

**Keywords:** gastrointestinal microrobot; expanding mechanism; elastodynamics; finite element analysis; structure optimization

## 1. Introduction

The morbidity and mortality of gastrointestinal malignancy and related diseases are increasing year by year, which has seriously threatened people's health and even life [1,2]. Traditional endoscopy has some problems, such as missed detection, the painful process, and potential to cause serious complications. Capsule endoscopy can only rely on the passive movement of intestinal peristalsis and cannot carry out fixed-point detection of the gastrointestinal tract. It also does not have the function of expanding the intestinal tract and cannot be examined at the intestinal fold [3]. Therefore, the research focused on the gastrointestinal microrobot which can move autonomically and expand the intestinal tract is important [4–8].

The expanding mechanism is the key device for the gastrointestinal microrobot (GMR) to achieve active locomotion and anchoring in the intestinal tract. The performance of the GMR is directly related to the gastrointestinal tract safety, applicability and work efficiency [9]. The robot must have enough safety, so as to avoid damage to the intestine. In addition, due to different size of the intestine in

different sections of the human body, a larger variable diameter ratio (VDR) can enable the robot to better diagnose the intestinal tract of different sections of the human body. Considering the actual operation conditions, in order to minimize the operation time, raising the locomotion efficiency of the robot is very important. The driven type of the expanding mechanism mainly includes the magnetic driven type [10–14] and the micromotor drive type [15–19]. The magnetically driven type expanding mechanism adopts an off-board power supply, which greatly reduces the power required by the on-board load. However, there are two problems with this type of mechanism. One is that it moves too fast, which makes it easy to cause impact on the intestinal tract. The other is that in practical application, real-time detection of robot posture is needed to apply the magnetic field in the corresponding direction, the technology is relatively complex. The advantage of the micromotor driving mode is that the action time is controllable, and there is no need to detect the robot posture, but the micromotor driving mode increases the power consumption of the board. Various institutions have developed different structural forms of expanding mechanism. The expanding mechanism designed by Chen W.W. et al. adopts the design of Archimedes' spiral leg [20,21]. Its expanding force increases with the increase of expanding radius, which conforms to the mechanical properties of the intestine, but the tip of its expanding arm is too sharp, and it is easy to get stuck in the intestinal tract when rotating, which is easy to cause damage to the intestinal tract. The airbag expanding mechanism [22,23] has a high level of safety for the gastrointestinal tract, but it takes too long to inflate and deflate, and its working mode is inefficient, which is not suitable for practical operation. The leg expanding mechanism designed by He S., Gao J.Y. et al. [24–26] takes into account the problems of movement efficiency and safety, but its VDR is relatively small (only 2.56), which is not suitable for the diagnosis of intestinal tract with a large diameter, and its expansion tension is small. The expanding mechanism developed by Zhou H. et al. [27] has a simple structure, but the VDR and the expanding force are small. To sum up, the main difficulties in the design of the expanding mechanism at present lie in the aspect of VDR, expanding force, and work efficiency.

In this paper, a novel expanding mechanism of the inchworm-like GMR is designed, which adopts a double-layer overlapping design and has a VDR of 3.3. The average time for the expanding mechanism to complete an expanding or folding action is about 1.2 s, which has a high working efficiency. At present, the research of expanding mechanism mainly focuses on the analysis of expanding force, anchoring force, and kinematics when the mechanism is regarded as a rigid body, and there are few studies on the dynamics of the expanding arm when it is deformed under load. In order to further study the correlation performance in the actual situation, it is necessary to analyze the elastodynamics of the expanding mechanism. Due to the relatively narrow intestinal tract of the human body, the size of the robot is strictly limited. Since the lighter and smaller the robot, the more flexible and locomotion efficient the mechanism in the intestinal tract, it is necessary to optimize the structure of the mechanism to make the robot lightweight and miniaturized.

## 2. Robot System

### 2.1. Structure of the Mechanism

The GMR system is mainly composed of four modules: the imaging module, the mechanical module, the wireless power receiving module, and the control circuit module, as shown in Figure 1. The imaging module is composed of a glass cover, a lens, LED light sources, a CMOS image sensor, and an image data wireless transmission circuit. The mechanical module is mainly composed of two expanding mechanisms and one telescoping mechanism and they are mainly made of titanium alloy. The wireless power receiving module is mainly composed of a receiving coil and a rectifying circuit.

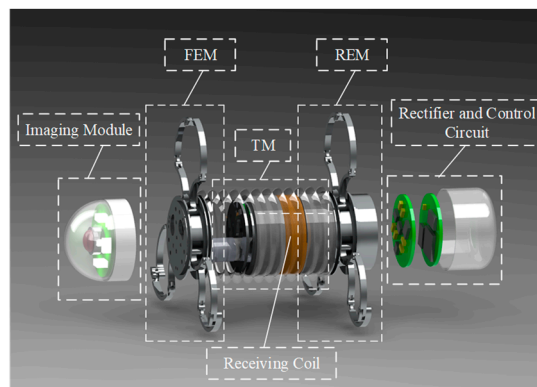


**Figure 1.** The structure of robot system.

The mechanical structure of the robot mainly consists of three parts: the front expanding mechanism (FEM), the rear expanding mechanism (REM), and the telescoping mechanism (TM). The FEM and REM have the same structure, the FEM moves relative to the TM, and the REM is fixed to the TM. The expanding mechanism is mainly composed of a driving device, a transmission device and three sets of expanding arms. The driving device is composed of a hollow cup motor and a reducer. The reducer adopts a 5-layer planetary gear type structure, and the reduction ratio of each layer is 4. The transmission device is mainly composed of three sets of external meshing gears. There are three sets of expansion arms, each consisting of four curved connecting rods.

The structure of the expanding mechanism of GMR is shown in Figure 2. The main component names: (1) Top panel, (2) Middle panel, (3) Gear pair of expanding arm, (4) Drive gear, (5) Transmission shaft of expanding arm, (6) Expanding arm, (7) Bolt, (8) Pedestal, (9) Bottom panel, (10) Motor and reducer.

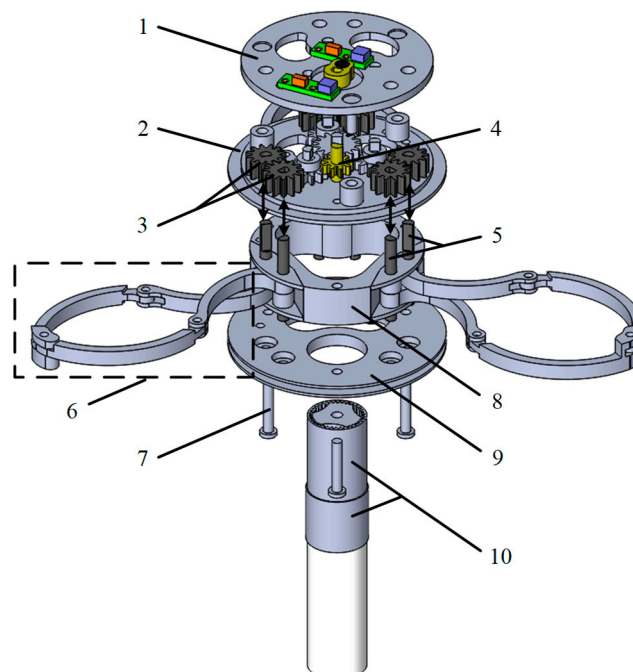


**Figure 2.** Structure of the expanding mechanism.

The motor provides driving force, the torque is reduced by the reducer, the force is transmitted to the transmission gear set, and then the transmission shaft is driven to rotate by the transmission gear set, thereby driving the expanding arm to achieve expanding and folding. The expanding arm is in contact with the intestinal tract during the expansion process. The larger the expanding radius is, the greater

the resistance will be, resulting in the larger the current of the control circuit. It is assumed that: (1) the mechanical properties of various parts of the human digestive tract are the same, (2) the motor performance remains stable all the time. The upper limit of current is set in the control circuit through in vitro intestinal experiment. Once the upper limit of the current is exceeded, the expanding arm will stop expanding, so as to avoid damage to the intestinal tract caused by excessive expanding force.

The relevant parameters of the expanding mechanism are shown in Table 1.

**Table 1.** Parameters of mechanical structure.

Parameter		Value
Expanding Mechanism	Size (folded)	$\Phi 15 \times 6.5$ mm
	Size (expanded)	$\Phi 49 \times 6.5$ mm
	VDR	3.3
	Reducer & Motor	$\Phi 4 \times 19.8$ mm
	Reduction ratio	1024

### 2.2. Locomotion Principle

The locomotion principle is shown in Figure 3. Two expanding mechanisms of the GMR alternately expand and fold. The screw-nut pair of the telescoping mechanism drive the folded expanding mechanism to move, thereby the robot moves in the intestinal tract. Step 0: The FEM and REM are folded. Step 1: The REM expands. Step 2: The screw-nut pair drive the FEM to move forward. Step 3: The FEM expands first, and then the REM folds. Step 4: The screw-nut pair drive the REM to move forward. The inchworm-like GMR repeats the Step 1–4, thus moves forward.

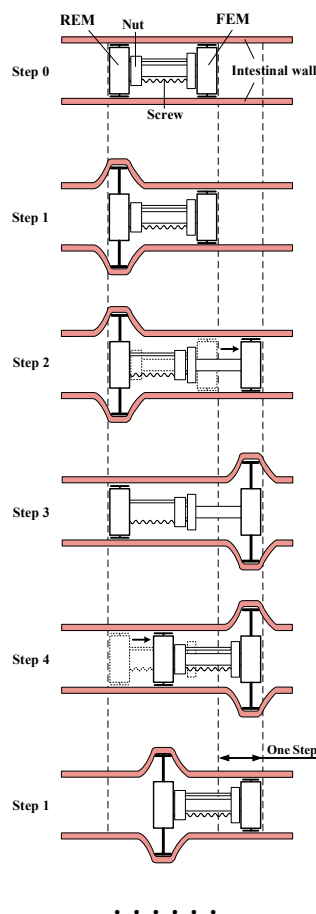


**Figure 3.** Locomotion principle of the inchworm-like GMR.

### 3. Kinematics and Mechanics Analysis of the Expanding Arm

#### 3.1. Kinematics Analysis

For rigid body kinematics analysis of the expanding arm, the expanding arm is simplified into a slider-crank mechanism module, as shown in Figure 4. Create a Cartesian coordinate system  $Oxy$  with the center of the mechanism  $O$  as the origin, and define the coordinates of the hinge points  $O_1(x_1, y_1)$ ,  $M(x_2, y_2)$ ,  $P(x_3, y_3)$ .

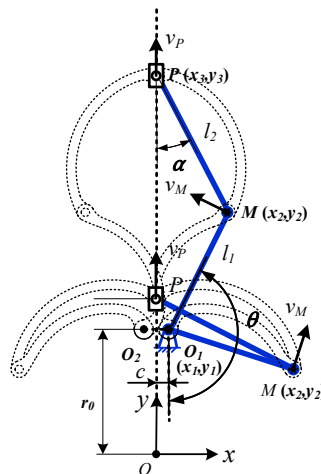


Figure 4. Kinematics analysis of the expanding arm.

The mathematical model of the hinge point coordinate matrix  $S$  is as follows:

$$S = \begin{bmatrix} x_1 & y_1 \\ x_2 & y_2 \\ x_3 & y_3 \end{bmatrix} \tag{1}$$

The constraint equation is:

$$\begin{cases} x_2 - x_1 = l_1 \cdot \sin \theta \\ y_2 - y_1 = -l_1 \cdot \cos \theta \\ x_3 - x_2 = -l_2 \cdot \sin \alpha \\ y_3 - y_2 = l_2 \cdot \cos \alpha \\ l_1 \cdot \sin \theta + x_1 = l_2 \cdot \sin \alpha \end{cases} \tag{2}$$

where,  $l_1, l_2$  are the lengths of the rod  $O_1M$  and the rod  $MP$ , respectively;  $\theta, \alpha$  are the angles of the rod  $O_1M$  and the rod  $MP$  with the vertical direction, respectively.

The point  $O_1$  is a fixed point, let  $x_1 = c, y_1 = r_0$ , and  $c, r_0$  is constant. Then in the  $Oxy$  coordinate system, the mathematical model of each hinge point coordinate matrix is:

$$S = \begin{bmatrix} x_1 & y_1 \\ x_2 & y_2 \\ x_3 & y_3 \end{bmatrix} = \begin{bmatrix} c & r_0 \\ l_1 \cdot \sin \theta + c & -l_1 \cdot \cos \theta + r_0 \\ 0 & Q - l_1 \cdot \cos \theta + r_0 \end{bmatrix} \tag{3}$$

where,  $Q = \sqrt{l_2^2 - (l_1 \cdot \sin \theta + c)^2}$ .

The first and second derivatives of coordinate matrix  $S$  with respect to time  $t$  are velocity matrix  $V$  and acceleration matrix  $A$  of each hinge point respectively.

$$V = \begin{bmatrix} \dot{x}_1 & \dot{y}_1 \\ \dot{x}_2 & \dot{y}_2 \\ \dot{x}_3 & \dot{y}_3 \end{bmatrix} = \omega \begin{bmatrix} 0 & 0 \\ l_1 \cdot \cos \theta & l_1 \cdot \sin \theta \\ 0 & l_1 \cdot \sin \theta - l_1 \cdot \cos \theta \cdot \frac{l_1 \cdot \sin \theta + c}{Q} \end{bmatrix} \tag{4}$$

$$A = \begin{bmatrix} \ddot{x}_1 & \ddot{y}_1 \\ \ddot{x}_2 & \ddot{y}_2 \\ \ddot{x}_3 & \ddot{y}_3 \end{bmatrix} = \omega^2 \begin{bmatrix} 0 & 0 \\ -l_1 \cdot \sin \theta & l_1 \cdot \cos \theta \\ 0 & l_1 \cdot \cos \theta + l_1 \sin \theta \cdot \frac{l_1 \cdot \sin \theta + c}{Q} - \frac{l_1^2 \cdot l_2^2 \cdot \cos^2 \theta}{Q^3} \end{bmatrix} \tag{5}$$

It is the angular velocity of the rod  $O_1M$ .

According to the above Equations (1)–(5), the expanding radius  $r_c$  and the velocity and acceleration of point  $P$  can be obtained. As follows:

$$\begin{cases} r_c = y_3 \\ v_p = \sqrt{\dot{x}_3^2 + \dot{y}_3^2} \\ a_p = \sqrt{\ddot{x}_3^2 + \ddot{y}_3^2} \end{cases} \tag{6}$$

The relevant design parameters of the expanding mechanism are shown in Table 2.

**Table 2.** Design parameters of mechanism.

Parameter	Value
$l_1/\text{mm}$	8.50
$l_2/\text{mm}$	10.70
$r_0/\text{mm}$	5.66
$c/\text{mm}$	1.20
$\omega/\text{rad/s}$	1.70

At different expanding radii  $r_c$  ( $7.5 \text{ mm} \leq r_c \leq 24.5 \text{ mm}$ ), the velocity  $v_p$  and acceleration  $a_p$  of point  $P$  are shown in Figure 5. When the expanding radius  $r_c = 10.0 \text{ mm}$ , the absolute value of acceleration at point  $P$  reaches the maximum,  $|a_p|_{\text{max}} = 53.12 \text{ mm}^2/\text{s}$ . When the expanding radius  $r_c = 15.2 \text{ mm}$ , the point  $P$  velocity reaches the maximum,  $v_{p\text{max}} = 22.28 \text{ mm/s}$ .

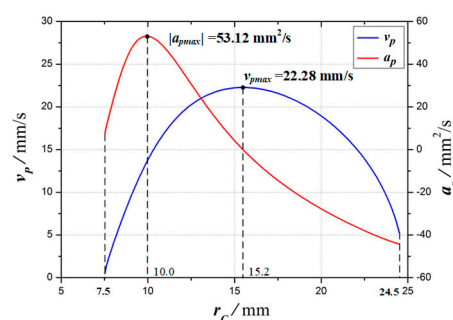


**Figure 5.** Theoretical velocity and acceleration of point  $P$ .

### 3.2. Expanding Force Analysis

For expanding force analysis of the expanding mechanism, the expanding arm can be considered as a static system, as shown in Figure 6.

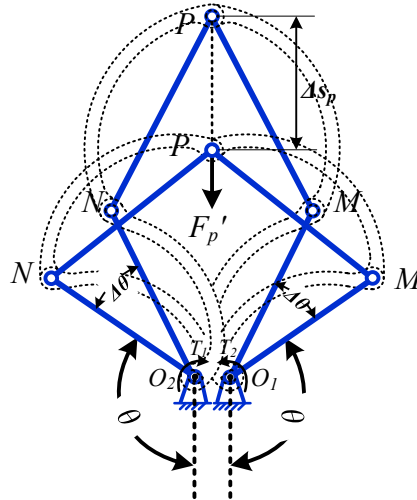


Figure 6. Mechanical analysis of the expanding arm.

According to the principle of virtual work, the virtual work done by the moments  $T_1$  and  $T_2$  on the small-angle increment  $\Delta\theta$  is  $T_1 \cdot \Delta\theta$  and  $T_2 \cdot \Delta\theta$ , respectively.

$$\begin{cases} T_1 \cdot \Delta\theta + T_2 \cdot \Delta\theta - F'_P \cdot \Delta s_p = 0 \\ T = T_1 + T_2 \end{cases} \quad (7)$$

From Equation (3):

$$\Delta s_p = \left( l_1 \cdot \sin \theta - l_1 \cdot \cos \theta \frac{(l_1 \cdot \sin \theta + c)}{\sqrt{l_2^2 - (l_1 \cdot \sin \theta + c)^2}} \right) \cdot \Delta\theta \quad (8)$$

According to Equations (7),(8), the expanding force  $F_P$  can be derived:

$$F_P = F'_P = T \cdot \left( l_1 \cdot \sin \theta - l_1 \cdot \cos \theta \frac{(l_1 \cdot \sin \theta + c)}{\sqrt{l_2^2 - (l_1 \cdot \sin \theta + c)^2}} \right)^{-1} \quad (9)$$

where,  $r_c$  is the radius of expanding;  $F_P$  and  $F'_P$  are the expanding force and reaction force at point  $P$ ;  $T_1$  and  $T_2$  are the maximum driving torques acting on  $O_1$  and  $O_2$ , respectively;  $T$  is the maximum driving torque of the expanding arm under the rated voltage of the motor, the value is tested to be 32 N·mm.

According to Equations (1) and (9), the relationship between the expanding force at point  $P$   $F_P$  and the expanding radius  $r_c$  can be obtained, as shown in Figure 7. As the mechanism arm expands, the expanding force  $F_P$  first gets smaller and then larger. When  $r_c = 7.5$  mm (the fully folded state of the expanding arm),  $F_P$  is the maximum,  $F_{Pmax} = F_P(7.5) = 28.498$  N. After that,  $F_P$  sharply decreases.  $F_P$  changes relatively small when  $r_c$  is from 10 mm to 22 mm. When  $r_c = 15.3$  mm,  $F_P$  is the minimum,  $F_{Pmin} = F_P(15.3) = 2.381$  N. When  $r_c = 24.5$  mm (the fully expanded state of the expanding arm),  $F_P(24.5) = 9.534$  N.





strength, the maximum thickness of the monolayer expanding arm should be 1.2 mm before in-depth strength analysis.

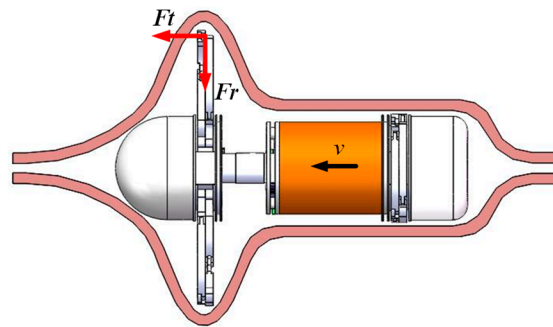


Figure 9. The force condition of GMR in the intestine.

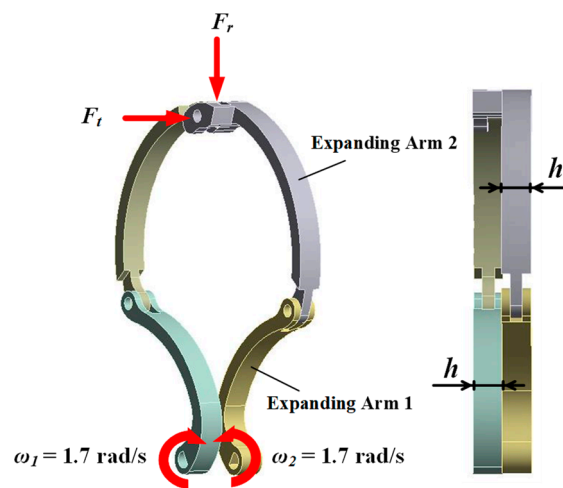


Figure 10. Load applied to the expanding arm.

The equivalent stress distribution of the expanding arm is shown in Figure 11. Figure 12 shows the maximum equivalent stress values of the expanding arms 1 and 2 with different expanding radii. It can be seen that with the expansion of the expanding arm, the maximum equivalent stress appears alternately on the expanding arm 1 and 2. The maximum equivalent stress of the whole motion process appears on expanding arm 2 in the initial expanding phase and the maximum value  $\sigma_{\max} = 428.53$  MPa. The material of the expanding arm is Ti-6Al-4V ELI, its yield strength  $\sigma_s = 950$  MPa. The safety factor [s] is set to 1.1, so the safety stress of expanding arm is  $\sigma_{[s]} = \sigma_s/[s] = 864$  MPa. As  $\sigma_{\max} < \sigma_{[s]}$ , the strength of expanding arm meets requirements.

Based on the FEA, the response of the velocity  $v_{pf}$  and the acceleration  $a_{pf}$  of point  $P$  is compared with the theoretical value  $v_p$  and  $a_p$  as shown in Figure 13a,b. As can be seen from the figure, the velocity and acceleration of the expanding arm fluctuate greatly in three stages, namely  $r_c = 7.5$  mm stage,  $r_c = 8.5\text{--}9.7$  mm stage, and  $r_c = 22.8\text{--}24.0$  mm stage. The corresponding maximum deviation values of velocity  $|\Delta v|_{\max}$  and acceleration  $|\Delta a|_{\max}$  are shown in Table 3. From the comparison between Figures 12 and 13, it can be seen that when the stress mutation occurs in the expanding arm, the velocity and acceleration of point  $P$  will fluctuate.

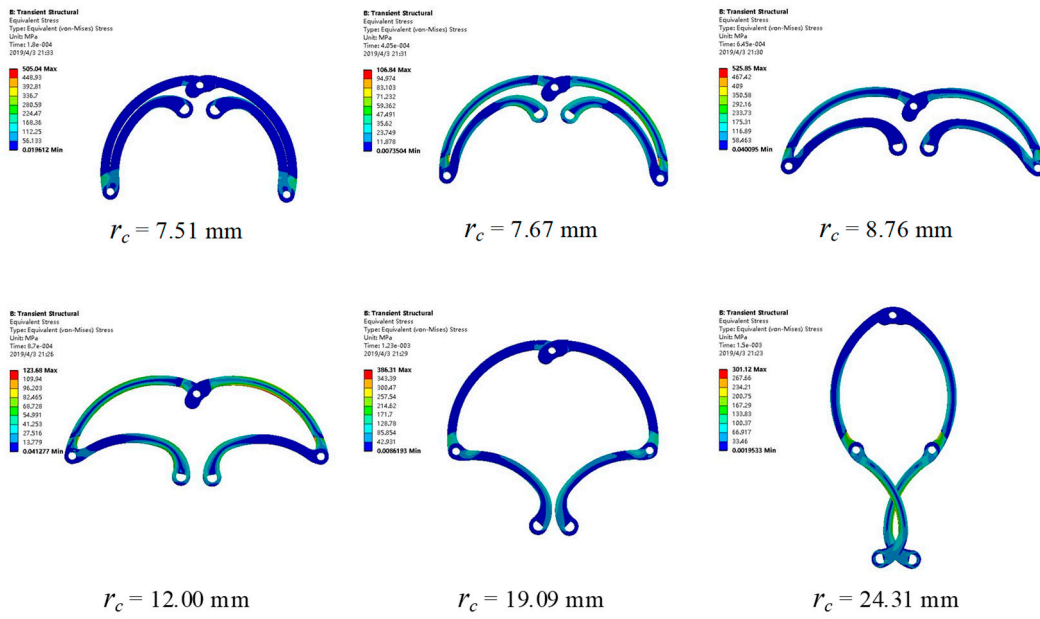


Figure 11. The equivalent stress of expanding arm.

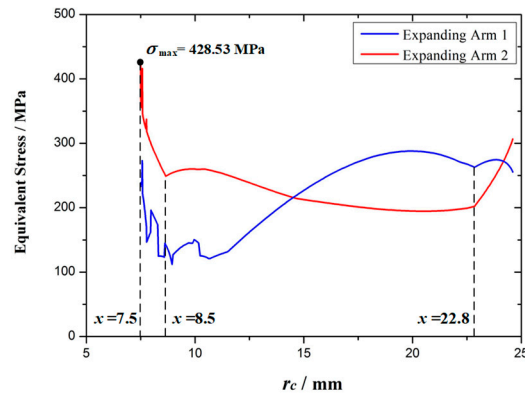


Figure 12. The curves of the equivalent stress.

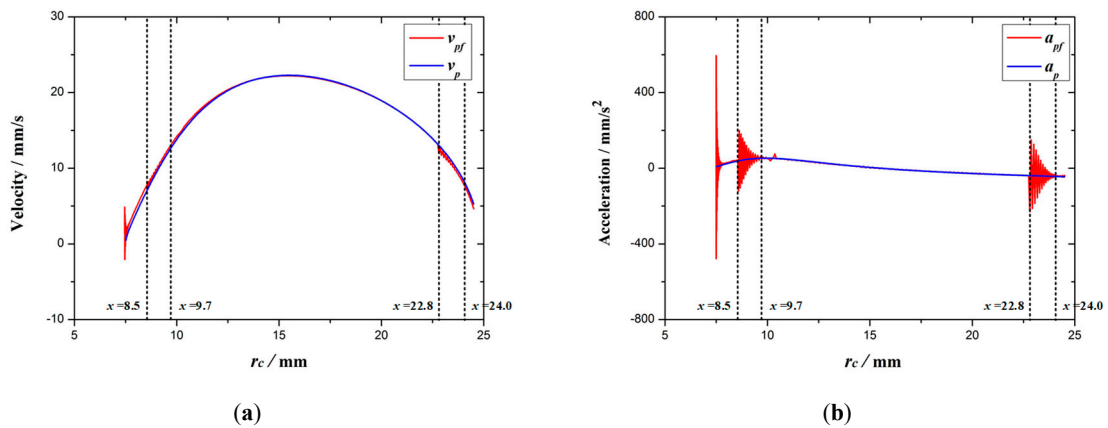


Figure 13. The response curves of velocity (a) and acceleration (b).

**Table 3.** Maximum amplitude of velocity and acceleration with different expanding radius.

$r_c$ /(mm)	$ \Delta v _{\max}$ /(mm/s)	$ \Delta a _{\max}$ /(mm/s <sup>2</sup> )
7.5	4.81	587.00
8.5–9.7	0.80	158.81
22.8–24.0	0.94	189.97

#### 4.3. Structure Optimization of the Expanding Arm

As can be seen from the above FEA, the maximum stress of the expanding arm is far less than the safe stress, and the stress is mainly concentrated at the joint of each arm and the edge of the expanding arm, so the structure of the expanding arm needs to be optimized.

The thickness of the expanding arm is first optimized. The maximum equivalent stress is less than the safe value as the boundary condition. The thickness of the expanding arm is used as the optimization variable. The objective of the optimization is to minimize the thickness of the expansion arm. As shown in the following formula:

$$\begin{cases} h_i = 1.2, 1, 0.8 \dots \text{mm} (i = 1, 2, 3 \dots) \\ \sigma_{\max-h} \leq \sigma_{[s]} \\ \min(h) \end{cases} \quad (12)$$

where  $h_i$  is the thickness of the expanding arm,  $\sigma_{\max-h}$  is the maximum equivalent stress of the expanding arm with different thicknesses. The FEA is carried out on the expanding arms with different thickness respectively to obtain the maximum equivalent stress in the whole movement process, as shown in Table 4. It can be seen from Table 4 that when the thickness of the expanding arm is 0.8 mm, the stress of the expanding arm does not meet the safety requirement, so the thickness of the expanding arm is optimal when it is 1 mm.

**Table 4.** The maximum equivalent stress with different thickness.

$h_i$ /(mm)	$\sigma_{\max}$ /(Mpa)	$\sigma_{[s]}$ /(Mpa)
1.2	428.50	864
1.0	510.94	864
0.8	917.02	864

It can be seen from the stress distribution of the expanding arm that the stress in the middle region is much less than the stress in the edge region. The structure optimization of expanding arm 1 and 2 is carried out respectively. First, hollow out the middle region of the expanding arm. Then, the middle region of the expansion arm is divided into segments 1, 2, 3... until the maximum equivalent stress of the expanding arm is less than the safety stress. The optimization process is shown in Figure 14. From the analysis results, it can be concluded that the stress of the hollow part of expanding arm 1 and 2 meets the safety requirements when they are divided into three segments.

Figure 15 shows the equivalent stress curve of the optimized expanding arm 1 and 2 during the movement. It can be seen that the stress of the optimized expanding arm is increased, and the overall maximum equivalent stress appears on the expanding arm 1, the maximum value  $\sigma'_{\max} = 852.47$  MPa  $< \sigma_{[s]} = 864$  MPa, it meets the requirements of safety strength.

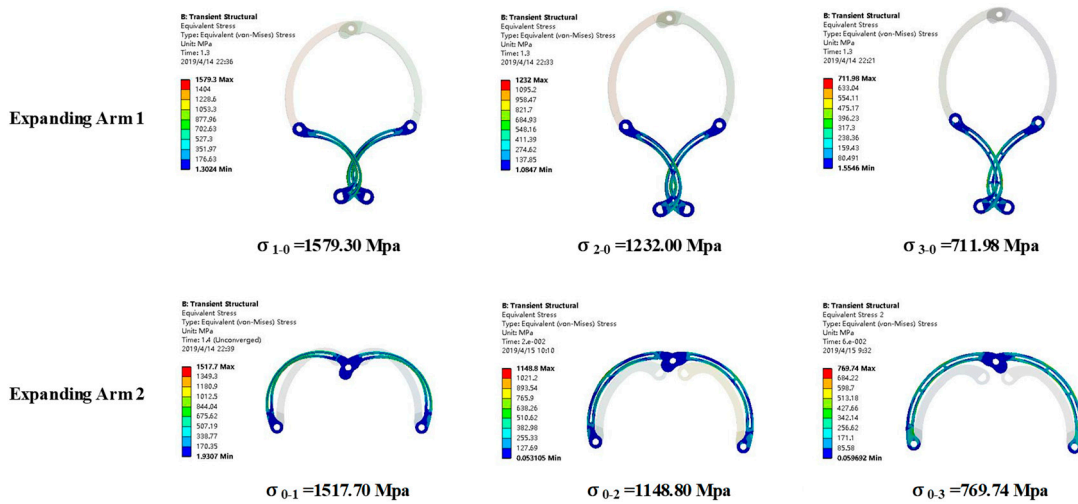


Figure 14. Optimization process of the expanding arm.

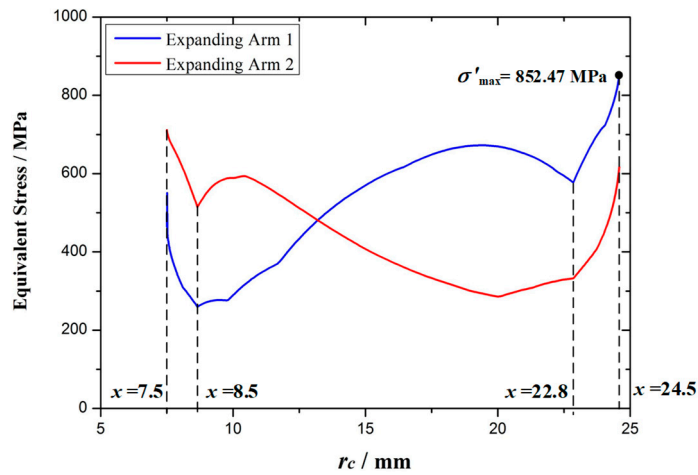


Figure 15. The equivalent stress of the optimized expanding arm.

The comparison between the velocity  $v'_{pf}$  and acceleration  $a'_{pf}$  at point  $P$  of the optimized expanding arm and the theoretical value is shown in Figure 16a,b. As before structural optimization, the velocity and acceleration of the optimized expanding arm fluctuate greatly in three stages. The corresponding maximum deviation values of velocity  $|\Delta v|_{max}$ , and acceleration  $|\Delta a|_{max}$  are shown in Table 5. Affected by the increase of stress, the fluctuation of velocity and acceleration at point  $P$  of expanding arm also increases.

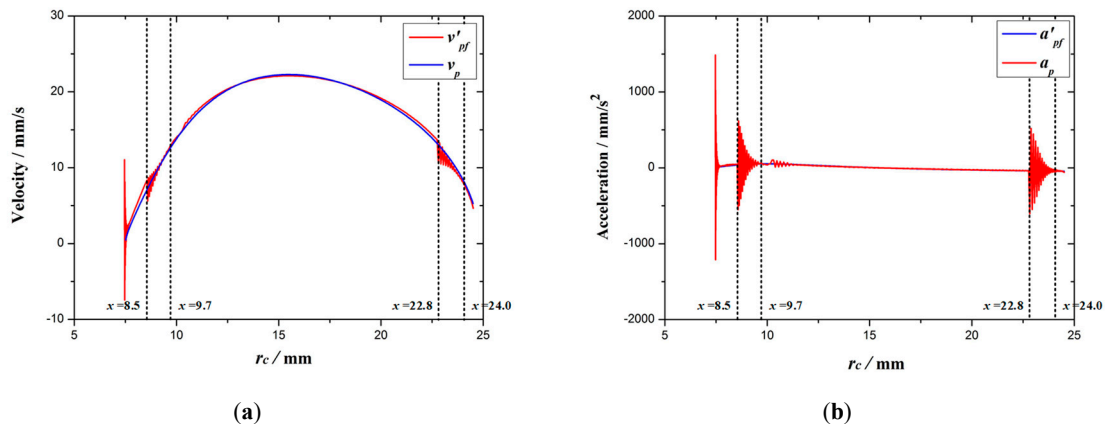
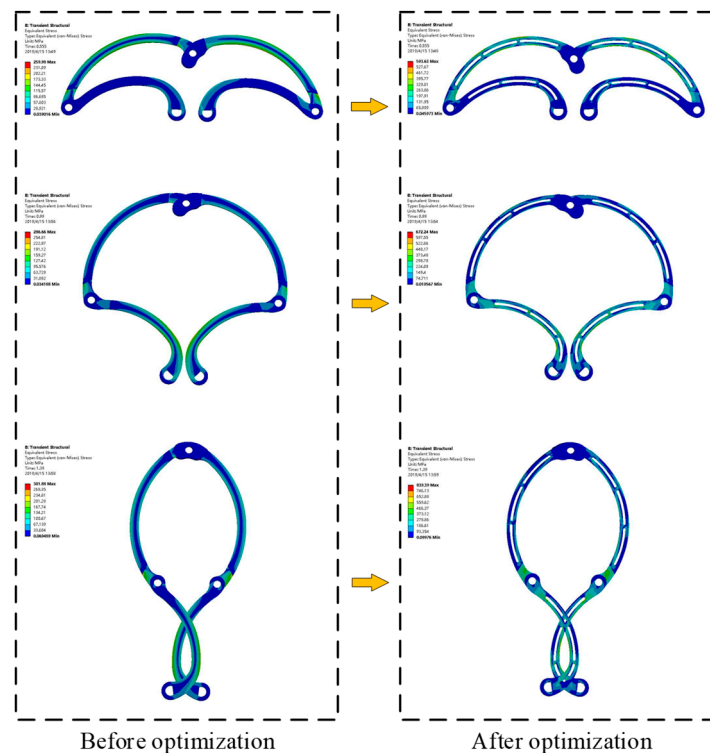


Figure 16. The response curves of velocity (a) and acceleration (b) after optimization.

**Table 5.** The maximum amplitude of velocity and acceleration with different expanding radius.

$r_c$ /(mm)	$ \Delta v _{\max}$ /(mm/s)	$ \Delta a _{\max}$ /(mm/s <sup>2</sup> )
7.5	10.56	1478.39
8.5–9.7	1.53	589.32
22.8–24.0	2.32	566.00

Figure 17 shows the comparison of equivalent stress with different expanding radii before and after the expansion arm optimization. After optimization, the overall thickness of the expanding arm is reduced by 0.4 mm, the weight of expanding arm is reduced by 31%.

**Figure 17.** Comparison of stress distribution before and after optimization.

## 5. Experiment

### 5.1. Expanding Force Test

According to theoretical analysis, the expanding force is large in the fully folded stage, which may cause intestinal damage. Therefore, a mechanical test platform is built to test the actual expanding force of the expanding mechanism, as shown in Figure 18. The test platform consists of the DC power supply, dynamometer, control switch, clamping device, and base. The expanding mechanism is fixed on the clamping device, and the knob on the clamping device is used to adjust the distance between the expanding mechanism and the probe of the dynamometer, so as to measure the expanding force under different expanding radius. The control switch is used to control the forward and reverse of the motor and to protect the motor.

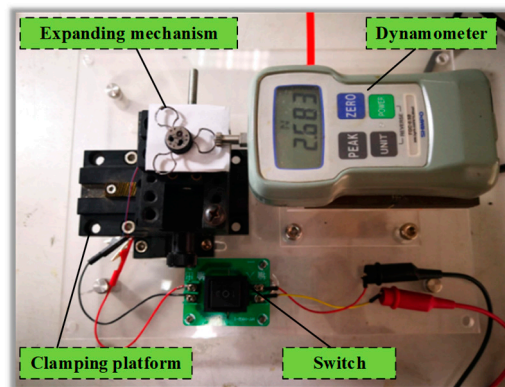


Figure 18. Mechanical performance test platform.

Based on this platform, the expanding forces of the expanding arms 1, 2 and 3 are tested at the interval of 1 mm and the limit positions of 7.5 mm and 24.5 mm respectively. Each group of expanding arms is tested three times, and the average value is obtained. The experimental and theoretical curves of the expanding forces of the three groups of expanding arms are compared, as shown in Figure 19.

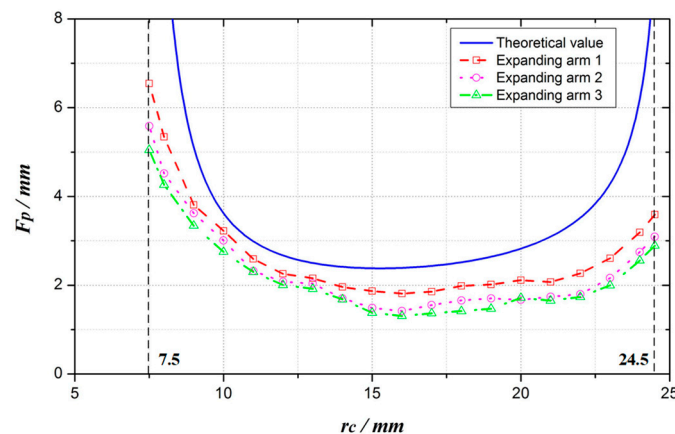


Figure 19. Experimental and theoretical value of expanding force.

The analysis of the experimental results is as follows:

The three groups of experimental curves have the same trend as the theoretical curves, and the experimental values are less than the theoretical values. This is due to the efficiency of gear transmission and friction loss between mechanisms.

The maximum experimental value of three groups of expanding arms is 6.5 N, and the minimum experimental value is 1.3 N. The expanding force of expanding arm 1 is larger than that of expanding arm 2 and 3. In the process of installation, the running-in degree and transmission gear of expanding arm 1 is better than that of expanding arm 2 and 3, and the friction resistance is smaller in the course of motion, so that the expanding force is larger than that of the other two groups.

When the expanding radius is from 7.5 mm to 10 mm and from 22 mm to 24.5 mm, the slope of the curve is larger so that the small disturbance will cause a huge error to the expanding force, so the error between the experimental value and the theoretical value is larger. When the expanding radius is 10 mm to 22 mm, the curve is relatively stable and the error is relatively small. The average experimental value of the expansion arm 1 is 79.30% of the theoretical value, the expansion arm 2 is 68.04%, and the expansion arm 3 is 63.90%.

## 5.2. Locomotion Experiment

In order to verify the reliability and safety of the optimized mechanism, the robot is placed in a rigid tube (acrylic tube) and an isolated intestine (pig small intestine) for the locomotion experiment, as shown in Figure 20a–f. Figure 20a–c show the robot moving in the rigid pipe, and Figure 20d–f show the robot moving in the in vitro intestinal tract. During the locomotion of the robot, the mechanism works stably and reliably, and there is no obvious bending deformation of the expanding arm and no obvious damage to the intestine by a visual check. The average velocity of the robot in rigid tubes is 1.21 mm/s, while that in in vitro intestines was 0.94 mm/s. The velocity of the robot in the isolated intestine was significantly lower than that in the rigid tube. This is because the robot will lose step when it locomotes in the intestine. The main reasons for step loss are as follows:

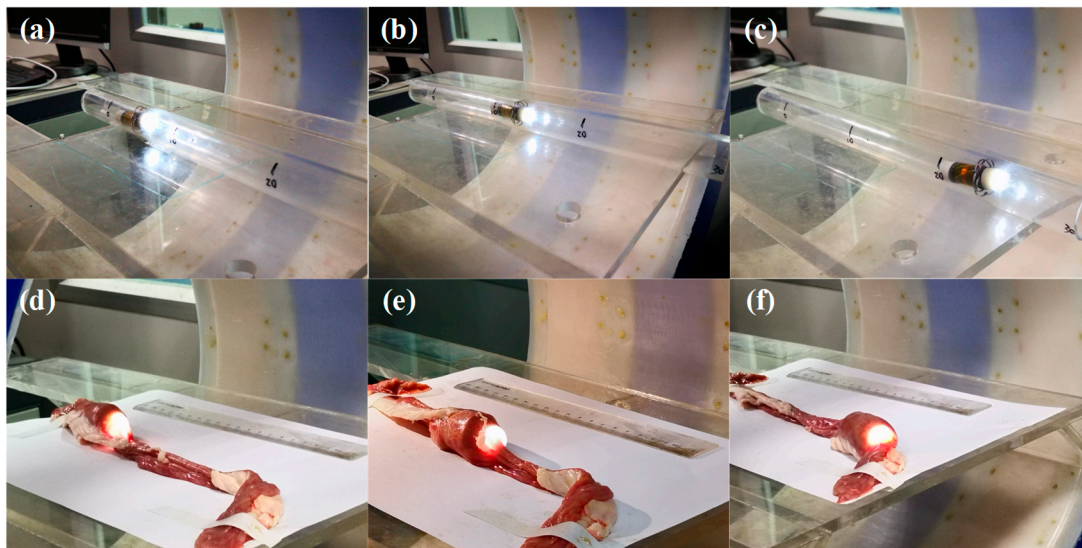


**Figure 20.** Robot locomotion experiment in the rigid pipe (a–c) and isolated intestine (d–f).

The intestinal tract is malleable. As the robot locomotes in the intestine, the intestine will be elongated.

Compared with rigid pipes, the intestinal tract is relatively slippery. During the locomotion of the robot, there is slippage between the expanding mechanism and the intestinal tract, leading to the loss of step distance and the decrease of velocity.

## 6. Conclusion

In this paper, a novel GMR is proposed. Compared with other commercialized capsule endoscopy systems, the GMR proposed in this paper has the following advantages: (1) The GMR can achieve active locomotion in the intestinal tract so that the intestinal tract can be detected at a fixed point and the diagnostic efficiency can be improved. (2) The GMR has the function of expanding the intestinal tract so that the collapsed and folded areas of the intestinal tract can be seen to reduce missed detection. The double-layer overlapping structure of expanding arm increases the VDA of the mechanism and the contact area with the intestine, so that the robot has a certain improvement in reliability and safety to the gastrointestinal. Based on the elastodynamics analysis, a structure optimization method of the expanding arm is proposed. After optimization, the overall thickness of the expanding arm is reduced by 0.4 mm, the weight of expanding arm is reduced by 31%. Then the reliability and safety of the optimized expanding mechanism are proved by experiments. The results show that this optimization method is effective and this method can also be applied to the overall structure optimization of the GMR in the future.

However, there are still some problems with the robot. The structure of the GMR in this paper can be divided into two parts, one is composed of the imaging module and the front expanding mechanism, and the other is composed of the rear expanding mechanism, the telescoping mechanism, the wireless power receiving module, and the control circuit module. There is a big difference in mass between the two parts, with the latter weight about twice as much as the former. This will decrease the locomotion efficiency of the robot. The emphasis of future work is to reduce the overall weight of the robot, optimize the weight distribution, and improve the locomotion efficiency of the robot.

**Author Contributions:** Conceptualization, W.W. and G.Y.; methodology, W.W.; software, W.W. and P.J.; investigation, Y.M. and Z.W.; data curation, F.C. and R.X.; writing—original draft preparation, W.W.; writing—review and editing, G.Y., Z.W. and P.J.

**Funding:** This research was funded by the National Natural Science Foundation of China (NSFC) (No. 61673271, No.81601631), Shanghai Science and Technology Support Project (No.19441910600, No.19441913800).

**Acknowledgments:** We also acknowledge our engineer Yinghua Gu for machining robot parts.

**Conflicts of Interest:** The authors declare no conflict of interest.

## References

1. Siegel, R.L.; Miller, K.D.; Jemal, A. Cancer statistics 2019. *CA A Cancer J. Clin.* **2019**, *69*, 7–34. [[CrossRef](#)] [[PubMed](#)]
2. Chen, W.; Zheng, R.; Baade, P.D.; Zhang, S.; Zeng, H.; Bray, F.; Jamel, A.; Yu, X.Q.; He, J. Cancer Statistics in China 2015. *CA A Cancer J. Clin.* **2016**, *66*, 115–132. [[CrossRef](#)] [[PubMed](#)]
3. Stein, D.J.; Shaker, R. Complications of upper gastrointestinal endoscopy. *Gastrointest. Emerg.* **2016**, *16*, 43–50.
4. Park, H.; Park, S.; Yoon, E.; Kim, B.; Park, J.; Park, S. Paddling based microrobot for capsule endoscopes. In Proceedings of the 2007 IEEE International Conference on Robotics and Automation, Roma, Italy, 10–14 April 2007; pp. 3377–3382.
5. Kim, H.M.; Yang, S.; Kim, J.; Park, S.; Cho, J.H.; Park, J.Y.; Kim, T.S.; Yoon, E.-S.; Song, S.Y.; Bang, S. Active locomotion of a paddling-based capsule endoscope in an in vitro and in vivo experiment (with videos). *Gastrointest. Endosc.* **2010**, *72*, 381–387. [[CrossRef](#)] [[PubMed](#)]
6. Zarrouk, D.; Shoham, M. Analysis and Design of One Degree of Freedom Worm Robots for Locomotion on Rigid and Compliant Terrain. *J. Mech. Des.* **2012**, *134*, 021010. [[CrossRef](#)]
7. Kim, B.; Lee, S.; Park, J.; Park, J.-O. Design and Fabrication of a Locomotive Mechanism for Capsule-Type Endoscopes Using Shape Memory Alloys (SMAs). *IEEE/ASME Trans. Mechatronics* **2005**, *10*, 77–86. [[CrossRef](#)]
8. Gorini, S.; Quirini, M.; Menciassi, A.; Pernorio, G.; Stefanini, C.; Dario, P. A Novel SMA-Based Actuator for a Legged Endoscopic Capsule. In Proceedings of the IEEE/RAS-EMBS International Conference on Biomedical Robotics and Biomechatronics, Pisa, Italy, 20–22 February 2006.
9. Wang, W.; Yan, G.Z.; Wang, Z.W.; Gao, J.Y.; Jiang, P.P.; Liu, D.S.; Zhao, K. Design and optimization of expanding mechanism of intestinal robot. *Opt. Precis. Eng.* **2017**, *25*, 1815–1824.
10. Simi, M.; Valdastri, P.; Quaglia, C.; Menciassi, A.; Dario, P. Design, Fabrication, and Testing of a Capsule With Hybrid Locomotion for Gastrointestinal Tract Exploration. *IEEE/ASME Trans. Mechatron.* **2010**, *15*, 170–180. [[CrossRef](#)]
11. Yim, S.; Sitti, M. Design and rolling locomotion of a magnetically actuated soft capsule endoscope. *IEEE Trans. Robot.* **2012**, *28*, 183–194. [[CrossRef](#)]
12. Zhang, Y.; Jiang, S.; Zhang, X.; Ruan, X.; Guo, D. A variable-diameter capsule robot based on multiple wedge effects. *IEEE/ASME Trans. Mechatron.* **2011**, *16*, 241–254. [[CrossRef](#)]
13. Kim, J.Y.; Kwon, Y.C.; Hong, Y.S. Automated alignment of rotating magnetic field for inducing a continuous spiral motion on a capsule endoscope with a twistable thread mechanism. *Int. J. Precis. Eng. Manuf.* **2012**, *13*, 371–377. [[CrossRef](#)]
14. Zhou, H.; Alici, G.; Than, T.D.; Li, W. Modeling and experimental investigation of rotational resistance of a spiral-type robotic capsule inside a real intestine. *IEEE/ASME Trans. Mechatron.* **2013**, *18*, 1555–1562. [[CrossRef](#)]
15. Wang, K.D.; Yan, G.Z.; Jiang, P.; Ye, D. A wireless robotic endoscope for gastrointestinal. *IEEE Trans. Robot.* **2008**, *24*, 206–210. [[CrossRef](#)]

16. Valdastri, P.; Webster III, R.J.; Quaglia, C.; Quirini, M.; Menciassi, A.; Dario, P. A new mechanism for mesoscale legged locomotion in compliant tubular environments. *IEEE Trans. Rob.* **2009**, *25*, 1047–1057. [[CrossRef](#)]
17. Woods, P.; Constandinou, T.G. Wireless capsule endoscope for targeted drug delivery: mechanics and design considerations. *IEEE Trans. Biomed. Eng.* **2013**, *60*, 945–953. [[CrossRef](#)]
18. Sliker, L.J.; Kern, M.D.; Rentschler, M.E. An automated traction measurement platform and empirical model for evaluation of rolling micropatterned wheels. *IEEE/ASME Trans. Mechatron.* **2015**, *20*, 1854–1862. [[CrossRef](#)]
19. Prendergast, J.M.; Formosa, G.A.; Rentschler, M.E. A Platform for Developing Robotic Navigation Strategies in a Deformable, Dynamic Environment. *IEEE Robot. Autom. Lett.* **2018**, *3*, 2670–2677. [[CrossRef](#)]
20. Chen, W.; Yang, G.; He, S.; Ke, Q. Clamping mechanism of capsule endoscopes in intestine. *Opt. Precis. Eng.* **2013**, *21*, 1553–1560. [[CrossRef](#)]
21. Chen, W.; Yan, G.; Wang, Z.; Jiang, P.; Liu, H. A wireless capsule robot with spiral legs for human intestine. *Int. J. Med Robot. Comput. Assist. Surg.* **2014**, *10*, 147–161. [[CrossRef](#)]
22. Gao, P.; Yan, G.; Wang, Z.; Wang, K.; Jiang, P.; Zhou, Y. A robotic endoscope based on minimally invasive locomotion and wireless techniques for human colon. *Int. J. Med. Robot. Comput. Assist. Surg.* **2011**, *7*, 256–267.
23. Yan, L.; Wang, T.; Liu, D.; Peng, J.; Jiao, Z.; Chen, C.Y. Capsule robot for obesity treatment with wireless powering and communication. *IEEE Trans. Ind. Electron.* **2015**, *62*, 1125–1133. [[CrossRef](#)]
24. He, S.; Yan, G.Z.; Ke, Q.; Wang, Z.W. Design and experiment of an intestinal anchoring mechanism. *Opt. Precis. Eng.* **2015**, *23*, 102–109.
25. Gao, J.Y.; Yan, G.Z. Locomotion analysis of an inchworm-like capsule robot in the intestinal tract. *IEEE Trans. Biomed. Eng.* **2016**, *63*, 300–310. [[CrossRef](#)] [[PubMed](#)]
26. Gao, J.; Yan, G.; Wang, Z.; He, S.; Xu, F.; Jiang, P.; Liu, D. Design and testing of a motor-based capsule robot powered by wireless power transmission. *IEEE/ASME Trans. Mechatron.* **2016**, *21*, 683–693. [[CrossRef](#)]
27. Zhou, H.; Alici, G.; Munoz, F. A magnetically actuated anchoring system for a wireless endoscopic capsule. *Biomed. Microdevices* **2016**, *18*, 102. [[CrossRef](#)]
28. Zhou, H.; Alici, G.; Munoz, F. Frictional and Viscous Characteristics of an Expanding-Extending Robotic Endoscope in the Intestinal Environment. *Tribol. Lett.* **2015**, *58*, 36.
29. Buselli, E.; Valdastri, P.; Quirini, M.; Menciassi, A.; Dario, P. Superelastic leg design optimization for an endoscopic capsule with active locomotion. *Smart Mater. Struct.* **2009**, *18*, 015001. [[CrossRef](#)]



© 2019 by the authors. Licensee MDPI, Basel, Switzerland. This article is an open access article distributed under the terms and conditions of the Creative Commons Attribution (CC BY) license (<http://creativecommons.org/licenses/by/4.0/>).